Research Article Vol. 30, No. 25 / 5 Dec 2022 / Optics Express 44741
Optics EXPRESS

High-precision magnetorheological finishing based on robot by measuring and compensating trajectory error

RUNMU CHENG,[1,2] LONGXIANG LI,[1,2,3] XINGCHANG LI,[1] BAI YANG,[1,2] XIAO LUO,[1] DONGLIN XUE,[1,2,4] AND XUEJUN ZHANG[1,2]

[1]*Changchun Institute of Optics, Fine Mechanics and Physics, Chinese Academy of Sciences, Changchun, Jilin 130033, China*
[2]*University of Chinese Academy of Sciences, Beijing 100049, China*
[3]*lilx@ciomp.ac.cn*
[4]*xuedl@ciomp.ac.cn*

Abstract: The 6-DOF industrial robot has wide application prospects in the field of optical manufacturing because of its high degrees of freedom, low cost, and high space utilisation. However, the low trajectory accuracy of robots will affect the manufacturing accuracy of optical components when the robots and magnetorheological finishing (MRF) are combined. In this study, aiming at the problem of the diversity of trajectory error sources of robot-MRF, a continuous high-precision spatial dynamic trajectory error measurement system was established to measure the trajectory error accurately, and a step-by-step and multistage iterations trajectory error compensation method based on spatial similarity was established to obtain a high-precision trajectory. The experimental results show that compared with the common model calibration method and general non-model calibration method, this trajectory error compensation method can achieve accurate compensation of the trajectory error of the robot-MRF, and the trajectory accuracy of the Z-axis is improved from $PV > 0.2$ mm to $PV < 0.1$ mm. Furthermore, the finishing accuracy of the plane mirror from 0.066λ to 0.016λ RMS and the finishing accuracy of the spherical mirror from 0.184λ RMS to 0.013λ RMS using the compensated robot-MRF prove that the robot-MRF has the ability of high-precision polishing. This promotes the application of industrial robots in the field of optical manufacturing and lays the foundation for intelligent optical manufacturing.

1. Introduction

With the popularity of segmented optics in next-generation telescopic systems such as the Giant Magellan Telescope [1], European-Extremely Large Telescope [2,3], and the Thirty Meter Telescope [4], among others, higher requirements have been proposed for the quantity, surface complexity, and quality of optical components in optical systems. However, it is challenging for traditional optical manufacturing to manufacture optical elements with high accuracy, high efficiency, and low cost. In recent years, an increasing number of industrial robots have been used to replace traditional CNC-machine to address these problems. A robot with a higher degree of freedom is more suitable for a complex surface; a lower use area is conducive to the placement of more robots, which is beneficial for improving efficiency; lower equipment cost is also positive to reduce expenses. Derst [5]et al. utilised a robot polisher manufacturing a 1560 mm on-axis asphere, and the surface quality at the end of the process was 0.045μm RMS. David Walker et al. [6] also utilised a robot to polish a large-aperture optical element that was assembled of 5-off 1 m A/C hexagonal float-glass sheets epoxied together. Other optical manufacturing technologies are used in combination with robots, such as robot-computer controlled optical surfacing [7,8], robot-wheeled polishing [9], and robot-bonnet polishing [10]. These studies indicate the diversity

#474959 https://doi.org/10.1364/OE.474959
Journal © 2022 Received 6 Sep 2022; revised 16 Oct 2022; accepted 17 Oct 2022; published 22 Nov 2022

Optics EXPRESS

of the combination of robot and optical manufacturing technologies and reveal the great potential of robot applications in optical manufacturing. However, due to the limitations of these optical manufacturing technologies themselves, such as polishing tool wear [11] and other reasons caused by the instability of the TIF, as well as the unique serial multi-joint structure of the robot leading to poor positioning precision and movement accuracy, as a result, the optical manufacturing equipment relying on the robot is more utilized in the grinding, pre-polishing and rough polishing and other manufacturing accuracy steps.

Magnetorheological finishing (MRF) [12–15] is a common optical manufacturing technology in the field of high-precision optical manufacturing, which has the advantages of a stable tool influence function (TIF) and high finishing certainty. However, the lower trajectory accuracy of the robot will cause TIF changes, which will affect the final polishing accuracy. Therefore, to achieve the goal of high-precision manufacturing, the most important aspect of robot-MRF is to improve its trajectory accuracy.

At present, the compensation methods for robot trajectory error mainly include model calibration [16,17] and non-model calibration methods [18–20]. For example, Bo Li et al. [21] used a neural-network-based approach to reduce the positioning error of the KUKA KR 500-3 robot from 1.879 mm to 0.227 mm. Combining geometric calibration and artificial neural network, Stefan Gadringer et al. [22] compensated COMAU Racer5-0.80 robot maximal positioning/orientation error to 0.605 mm/3.753 mrad, which is a reduction of 6.28%/7.41% of the error. It can be seen that the positioning accuracy [23–26] and trajectory accuracy [27,28] of the industrial robot can be significantly improved after compensation through the model calibration and non-model calibration methods. However, the calibration accuracy of these methods is mainly at sub-millimetre for large robots with a load of hundreds of kilograms and a motion range of more than 2 m, which is suitable for CCOS [29] and other optical manufacturing technologies that require relatively low trajectory accuracy. However, they cannot meet the requirements of trajectory precision in MRF high-precision polishing. To address this issue, this paper proposed a trajectory error compensation method based on multilevel iteration and step-by-step to achieve high-accuracy polishing trajectories. The method avoids modeling complex sources of robot trajectory error and can compensate for the path error caused by force variation between the mirror and the polishing tool during the polishing process. The omni-directional trajectory error compensation from the robot-MRF body to the polishing process was performed.

The key is to reduce the trajectory error of the equipment to improve the stability of the TIF and ensure the high-precision manufacturing capability of the robot-MRF. In this study, the influence of position and orientation errors on the gap stability of robot-MRF polishing is analysed. Aiming at the main influencing factors of polishing, an error-measuring platform based on a laser tracker was established, and the measurement error was eliminated. Furthermore, a trajectory error compensation method based on step-by-step and multistage iterations was proposed to obtain a high-precision trajectory for the robot-MRF. Finally, polishing experiments of planar and spherical mirrors were performed using the compensated robot-MRF.

2. Analysis of the influence of robot-MRF orientation and position error on polishing gap stability

A constant polishing gap is a premise for the high-precision polishing of MRF. When the robot-MRF is working, the positioning error and orientation error about the X-Y-Z axis will have different degrees of influence on the stability of the polishing gap. The relationship between the positioning/orientation error and polishing gap under different $R^{\#}$, where $R^{\#}=R/D$, R is the vertex radius of the elements, and D is the size of the elements, is as follows.

Optics EXPRESS

2.1. Analysis of influence of robot-MRF orientation error on polishing gap stability

This section analyses the relationship between the orientation error and the change in the polishing gap. It is assumed that the working point position of the polishing wheel remains unchanged, but the orientation changes. The relationship between the orientation error and the change in the polishing gap, in this case, is shown in Fig. 1, where h represents the theoretical polishing gap, h_v represents the corresponding polishing gap after the orientation change, l_1 represents the normal line corresponding to the point on the curve, θ represents the angle between the Z-axis and line l_1, θ_v represents the angle between the Z-axis and line l_1' after the orientation change, and the change in the polishing gap Δh is shown in Eq. (1) :

$$\Delta h = |h_v - h| \le \left| \frac{h}{\cos(\theta_v - \theta)} - h \right| = h \left| \frac{1}{\cos(\Delta\theta)} - 1 \right| \tag{1}$$

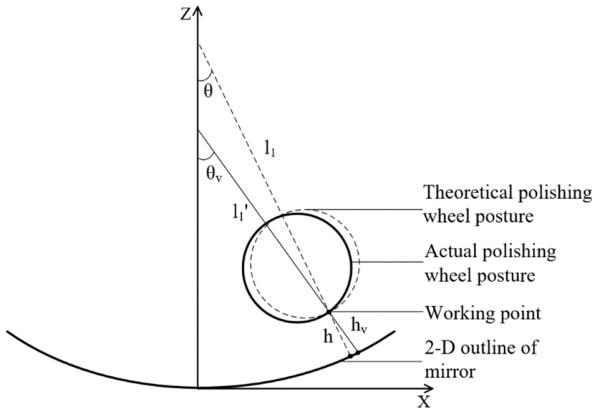

Fig. 1. The diagram of polishing wheel orientation and polishing gap change.

Equation (1) shows that the polishing gap change Δh is related to the polishing gap h and orientation angle change $\Delta\theta$, as shown in Fig. 2. Generally, the robot's orientation error is less than 1 ° [30,31], and its corresponding orientation error has an impact on the polishing gap of less than 0.5μm. Considering that the random error of industrial robots on the X-Y-Z axis is tens of microns to sub millimetres, the polishing gap variation caused by the orientation error will be covered by random error; thus, the orientation error can be ignored.

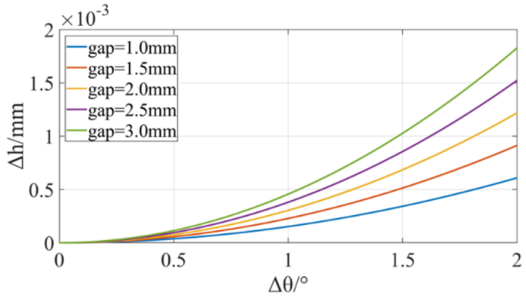

Fig. 2. The relation curve between orientation error and polishing gap variation.

Optics EXPRESS

2.2. Analysis of influence of robot-MRF positioning error on polishing gap stability

This section analyses the relationship between the positioning error and the change in the polishing gap. It is assumed that the working point orientation of the polishing wheel is unchanged, but the position changes. If the optical element is rotationally symmetric, its two-dimensional expression is given by Eq. (2).

$$z(x) = \frac{cx^2}{1 + \sqrt{1 - (k+1)c^2x^2}} + a_4x^4 + a_6x^6 + \cdots \tag{2}$$

Where c is the vertex curvature, k is the quadric coefficient, and a_4 and a_6 are high-order aspherical coefficients.

The relationship between the position error of the X-Z axis and the change in the polishing gap is shown in Fig. 3, where l_1 represents the normal line of theoretical points $W(x_w, z_w)$ on the curve, l_2 represents the tangent line of theoretical points $W(x_w, z_w)$ on the curve, l_3 represents the line that crosses $t(x_t, z_t)$ parallel to l_2, l_4 is parallel to l_1, point $t(x_t, z_t)$ represents the theoretical track point corresponding to the polished point $W(x_w, z_w)$, Δr represents the absolute positioning error of the robot-MRF in the X-Z axis direction, and the variation range of the positioning error is located in the circle centred at point $t(x_t, z_t)$ with radius Δr. The variation range of the polishing gap, h_v, is.

$$h - (\Delta h_1 + \Delta h_2) \le h_v \le h + (\Delta h_1 + \Delta h_2) \tag{3}$$

Where $\Delta h_1 = |CP|$, $\Delta h_2 = |MD|$.

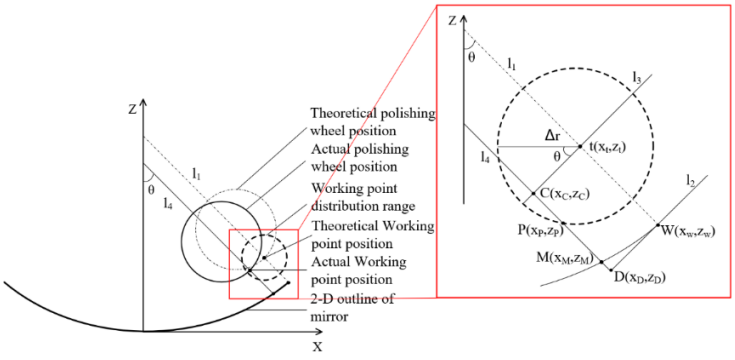

Fig. 3. The diagram of working point position of polishing wheel and polishing gap change.

Under the condition of constant orientation, the maximum value of the polishing gap change Δh is located at the edge of the circle $t(x_t, z_t)$, which is the point $P(x_P, z_P)$. Then, Δh_1 and Δh_2 can be expressed using Eq. (4) as follows:

$$\begin{cases} \Delta h_1 = \Delta x \sin\theta + \Delta z \cos\theta \\ \Delta h_2 = \sqrt{(x_D - x_M)^2 + (z_D - z_M)^2} \end{cases} \tag{4}$$

Optics EXPRESS

Where:

$$0 \le \Delta x \le \Delta r \cos\theta$$
$$\Delta r^2 = \Delta x^2 + \Delta z^2$$
$$\Delta x = x_P - x_t$$
$$\Delta z = z_P - z_t$$
$$\theta = \arctan(\tfrac{1}{A}) - \tfrac{\pi}{2}$$
$$A = z'(x) = \frac{cx}{1+\sqrt{1-(k+1)c^2x^2}} + 4a_4x^3 + 6a_6x^5 + \cdots$$

Point $D(x_D, z_D)$ indicates the intersection of lines l_2 and l_4; therefore, the coordinates of point $D(x_D, z_D)$ are expressed as Eq. (5) :

$$\begin{cases} x_D = x_w - l\cos\theta \quad |x_w| \le D/2 \\ z_D = z_w - l\sin\theta \\ l = \Delta x\cos\theta + \Delta z\sin\theta \end{cases} \tag{5}$$

Point $M(x_M, z_M)$ indicates the intersection of line l_4 and the curve, so the coordinates of point $M(x_M, z_M)$ are expressed as Eq. (6):

$$\begin{cases} -\frac{1}{A}x_M + B = \frac{cx_M{}^2}{1+\sqrt{1-(k+1)c^2x_M{}^2}} + a_4x_M{}^4 + a_6x_M{}^6 + \cdots \\ z_M = -\frac{1}{A}x_M + B \\ B = z_D + \frac{1}{A}x_D \end{cases} \tag{6}$$

Figure 3 shows that the $|\Delta h_1|$ corresponding to the intersection area under lines l_1 and l_3 represents the change in $|\Delta h_1|$ over the entire range of changes. Using the conic curve as an example to further simplify the analysis, Δh_1 and Δh_2 can be expressed as follows:

$$\Delta h_1 = \begin{cases} -\Delta x\sin\theta - \Delta z\cos\theta \quad \Delta x \ge 0 \\ \Delta x\sin\theta - \Delta z\cos\theta \quad \Delta x<0 \end{cases} \tag{7}$$

$$\Delta h_2 = \sqrt{(x_D - x_M)^2 + (z_D - y_M)^2} \tag{8}$$

Where:

$$\theta = \left|\arctan(\frac{1}{A}) - \frac{\pi}{2}\right|$$
$$A = z'(x) = \frac{cx}{\sqrt{1-(k+1)c^2x^2}}$$
$$B = z_D + \frac{1}{A}x_D = z_D - ax_D$$

$$x_D = \begin{cases} x_w - (\Delta x\cos\theta - \Delta z\sin\theta)\cos\theta \quad \Delta x \ge 0, |x_w| \le D/2 \\ x_w - (-\Delta x\cos\theta - \Delta z\sin\theta)\cos\theta \quad \Delta x \le 0, |x_w| \le D/2 \end{cases}$$
$$z_D = \begin{cases} z_w - (\Delta x\cos\theta - \Delta z\sin\theta)\sin\theta \quad \Delta x \ge 0, |x_w| \le D/2 \\ z_w - (-\Delta x\cos\theta - \Delta z\sin\theta)\sin\theta \quad \Delta x \le 0, |x_w| \le D/2 \end{cases}$$

Optics EXPRESS

$$\begin{cases} x_M = \frac{a-Bac(1+k)\pm\sqrt{a^2-Bc(-2+Bc(1+k))}}{c(1+a^2(1+k))} \\ z_m = ax_{\mathrm{M}} + B \end{cases}$$

Therefore, the variation in the polishing gap is related to the quadric surface coefficient k, aperture D of the optical element, vertex curvature c, and robot positioning error Δx. Thus, the contribution of the robot positioning error Δx to the polishing gap change at different Δh_x can be expressed as Eq. (9).

$$\Delta h_x = \begin{cases} -\Delta x \sin\theta - (x_D - x_M)\sin\theta & \Delta x \geq 0 \\ \Delta x \sin\theta - (x_D - x_M)\sin\theta & \Delta x < 0 \end{cases} \tag{9}$$

Using a spherical optical element ($k = 0$) as an example, the contribution Δh_x of the optical element steepness change to the polishing gap change under different Δx values is analysed. Set $D = 340$ mm, $R = 1/c \in [240.216, 3000]$ mm, $\Delta r = 0.346$ mm, $\Delta x \in [0.05, 0.2]$ mm. For different Δx values, the influence of the X-axis positioning error on the variation in the polishing gap with different $R^{\#}$ values are shown in Fig. 4 and Fig. 5. When $\arcsin(D/2R) = \arcsin(1/2R^{\#}) \leq 15°$, the X-axis positioning error leads to a change of polishing gap less than 0.05 mm, accounting for about 5% of the sum of the effects of X-axis and Z-axis positioning errors on the variation of polishing gap. The Y-axis positioning error has the same effect on the polishing gap variation when the Y-axis positioning error is similar to that of the X-axis. In this case, Z-axis positioning error Δz is the most important factor of polishing gap variation, accounting for approximately 90%, and the influence of positioning error of the X-axis and Y-axis on the variation in polishing gap is approximately 5% respectively, which has little effect on polishing accuracy and can be neglected.

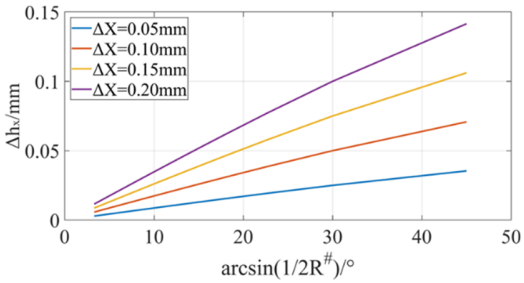

Fig. 4. Curves of $R^{\#}$ and Δh_x at different Δx values.

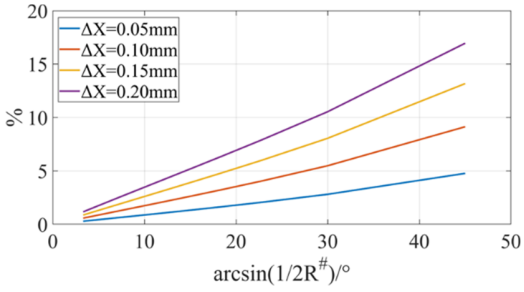

Fig. 5. Influence of different X-axis positioning error on the variation of polishing gap.

Optics EXPRESS

Based on Eq. (9), the influence of position error on the polishing gap is known when the orientation is unchanged. Therefore, the cooperative influence of the two factors can be express by Eq. (10).

$$\Delta h_x{}' = \begin{cases} -\Delta x \sin(\theta + \Delta\theta) - (x_D - x_M)\sin(\theta + \Delta\theta) & \Delta x \geq 0 \\ \Delta x \sin(\theta + \Delta\theta) - (x_D - x_M)\sin(\theta + \Delta\theta) & \Delta x < 0 \end{cases} \tag{10}$$

The influence of orientation/positioning error on the variation of the polishing gap as a function of different values of $R^{\#}$, when $\Delta\theta$=1 °, was shown in Fig. 6. The effect of orientation error on polishing gap under the combined action of the two factors can be expressed by Eq. (11), and the effect results were shown in Fig. 7 (a)and (b). The influence of orientation error on the polishing gap can be seen to be of the form Fig. 7 shows a gradual decrease with increasing steepness. Though the effect of orientation error on polishing gap is over 15% at $\arcsin(D/2R) = \arcsin(1/2R^{\#}) \leq 5°$, this has an effect on the polishing gap of less than 4 μm, and the effect of orientation error on the change in polishing gap is less than 6 μm over the entire range of variation in steepness in Fig. 7. The contribution of orientation error to the polishing gap can be negligible in comparison to the effect of position error on polishing gap. Therefore, accurate measurement and compensation of Z-axis trajectory error is the key to improving the trajectory accuracy of robot-MRF.

$$\begin{cases} \Delta h_{ori} = |\Delta h_x{}' - \Delta h_x| \\ P_{ori} = \left|\frac{\Delta h_x{}' - \Delta h_x}{\Delta h_x{}'}\right| \times 100\% \end{cases} \tag{11}$$

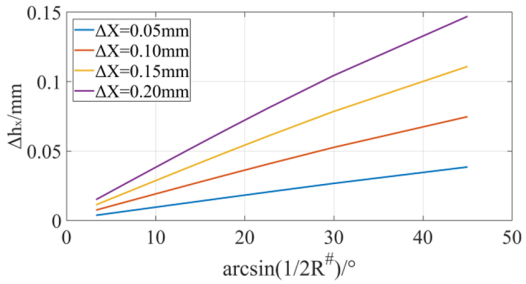

Fig. 6. Curves of orientation/position error and Δh_x at different Δx values.

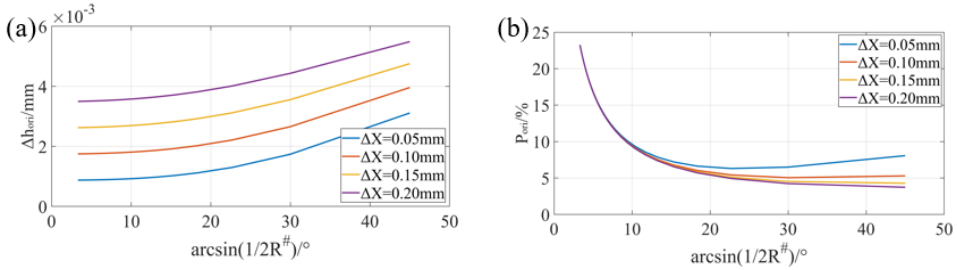

Fig. 7. (a) Curves of orientation error and Δh_{ori} at different Δx values, (b) the influence ratio of orientation error on the variation of polishing gap at different Δx values.

Optics EXPRESS

3. Robot-MRF trajectory error measurement and characteristic analysis

3.1. Construction of the robot-MRF trajectory error measurement system

Building a trajectory error measurement system is key to obtaining the robot-MRF trajectory error. Measuring the positioning/trajectory error of a robot with a laser tracker is one of the main methods for obtaining the positioning/trajectory error of a robot [32,33]. However, it is difficult for the laser tracker to directly measure the working point positioning/track error of the robot-MRF polishing wheel when the robot-MRF is in multi-motion, which means that the robot is running while the polishing wheel is rotating, and multi-pose, which means that the robot-MRF is in six-dimensional motion. Therefore, in this study, a continuous high-precision spatial dynamic method based on stiffness invariant characteristics was designed to measure the track error of the robot-MRF. The overall diagram of the robot-MRF measurement system is shown in Fig. 8.

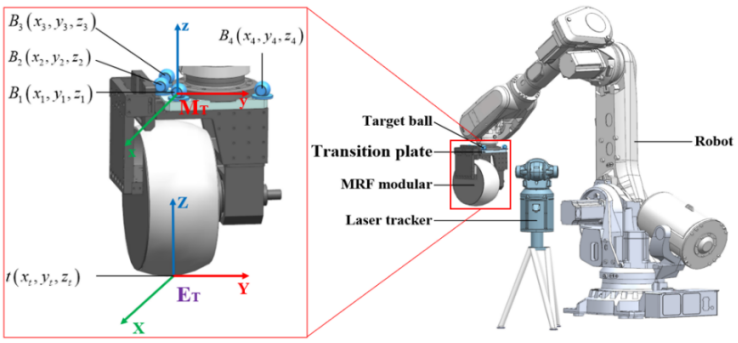

Fig. 8. The diagram of the robot-MRF trajectory error measurement system.

First, the measuring coordinate system M_T of the laser tracker is established. The target ball of the laser tracker is fixed at position $B_1(x_1, y_1, z_1)$ on the upper surface of the transition plate. The measuring coordinate system M_T of the laser tracker is established based on the robot-MRF end-tool coordinate system E_T, and they are parallel to each other. Because the distance between the target ball position $B_1(x_1, y_1, z_1)$ and polishing wheel working point $t(x_t, y_t, z_t)$ is constant, there is a fixed conversion relationship between them, as shown in Eq. (12).

$$W = \begin{bmatrix} R & P \\ 0 & 1 \end{bmatrix} \cdot B_1 \tag{12}$$

$R = R_z \cdot R_y \cdot R_x$ is the unit orthogonal rotation matrix representing the orientation transformation relationship between M_T and E_T, where R_z, R_y, and R_x represent the rotation transformation matrices around the Z, Y, and X axes, respectively. $P = [p_x, p_y, p_z]^T$ represents the position conversion relationship between M_T and E_T. Point $t(x_t, y_t, z_t)$ is in the tool coordinate system E_T, and point $B_1(x_1, y_1, z_1)$ is in the measurement coordinate system M_T. Therefore, Eq. (12) is converted to Eq. (13):

$$\begin{pmatrix} x_t \\ y_t \\ z_t \\ 1 \end{pmatrix} = \begin{bmatrix} a_x & b_x & c_x & p_x \\ a_y & b_y & c_y & p_y \\ a_z & b_z & c_z & p_z \\ 0 & 0 & 0 & 1 \end{bmatrix} \cdot \begin{pmatrix} x_1 \\ y_1 \\ z_1 \\ 1 \end{pmatrix} = T \cdot \begin{pmatrix} x_1 \\ y_1 \\ z_1 \\ 1 \end{pmatrix} \tag{13}$$

Optics EXPRESS

As shown in Eq. (13), as long as the 12 unknown parameters contained in the transformation matrix T are determined, the position $B_1(x_1, y_1, z_1)$ can be converted into the working point $t(x_t, y_t, z_t)$ of the polishing wheel, and the trajectory coordinates of the robot-MRF can be obtained.

Next, determine the conversion relation T between the position $B_1(x_1, y_1, z_1)$ and the polishing wheel working point $t(x_t, y_t, z_t)$. In addition to $B_1(x_1, y_1, z_1)$, at least two fixed positions are selected on the upper surface of the transition plate. The robot-MRF was set to at least 12 different orientations, and the coordinates of each position of $B_{ij}(x_{ij}, y_{ij}, z_{ij})(i \in N_+ \cap \max(i) \geq 2, j \in N_+ \cap \max(j) \geq 12)$ and at least four different positions $S_{jm}(x_{jm}, y_{jm}, z_{jm})(m \in N_+ \cap \max(m) \geq 4)$ of the polishing wheel surface were measured. The measured data are used to determine the transformation relationship T_i between the position $B_{1j}(x_{1j}, y_{1j}, z_{1j})$ and other positions $B_{ij}(x_{ij}, y_{ij}, z_{ij})$,as shown in Eq. (14) and the plane equation of the upper surface of the transition plate at different positions is determined, as shown in Eq. (15). The coordinates of the centre point $O_j(x_{j0}, y_{j0}, z_{j0})$ of the polishing wheel at different orientations were determined using the measured data $S_{jm}(x_{jm}, y_{jm}, z_{jm})$ and fitting ball function of the laser tracker.

$$T_i = \begin{bmatrix} a_{ix} & b_{ix} & c_{ix} & p_{ix} \\ a_{iy} & b_{iy} & c_{iy} & p_{iy} \\ a_{iz} & b_{iz} & c_{iz} & p_{iz} \\ 0 & 0 & 0 & 1 \end{bmatrix} = \begin{pmatrix} x_{ij} \\ y_{ij} \\ z_{ij} \\ 1 \end{pmatrix} \cdot \begin{pmatrix} x_{1j} \\ y_{1j} \\ z_{1j} \\ 1 \end{pmatrix}^{-1} \quad (i \neq 1) \tag{14}$$

$$A_j x + B_j y + C_j z + D_j = 0 \tag{15}$$

Third, determining the coordinates of the polishing wheel working point $t(x_t, y_t, z_t)$ under different poses. Figure 8 shows that the normal line of the transition plate passes through the centre point $O(x_0, y_0, z_0)$ and the working point $t(x_t, y_t, z_t)$ of the polishing wheel. The coordinate value of the working point $t(x_t, y_t, z_t)$ of the polishing wheel is solved using Eq. (16). Therefore, the coordinates of the working point $t(x_t, y_t, z_t)$ of the polishing wheel are shown in Eq. (17).

$$\begin{cases} \frac{x-x_{j0}}{A_j} = \frac{y-y_{j0}}{B_j} = \frac{z-z_{j0}}{C_j} \\ (x-x_{j0})^2 + (y-y_{j0})^2 + (z-z_{j0})^2 = R^2 \end{cases} \tag{16}$$

$$\begin{cases} X_j = (x_{j0} - b_1k_1 - b_2k_2 + k_1y_{j0} + k_2z_{j0} - (-{b_1}^2{k_2}^2 - {b_1}^2 + 2b_1b_2k_1k_2 - 2b_1k_1k_2z_{j0} - 2b_1k_1x_{j0} \\ \qquad +2b_1{k_2}^2y_{j0} + 2b_1y_{j0} - b_2{}^2{k_1}^2 - {b_2}^2 + 2b_2{k_1}^2z_{j0} - 2b_2k_1k_2y_{j0} - 2b_2k_2x_{j0} \\ \qquad +2b_2z_{j0} - {k_1}^2{x_{j0}}^2 - {k_1}^2{z_{j0}}^2 + R{k_1}^2 + 2k_1k_2y_{j0}z_{j0} + 2k_1x_{j0}y_{j0} - {k_2}^2{x_{j0}}^2 \\ \qquad -{k_2}^2{y_{j0}}^2 + R{k_2}^2 + 2k_2x_{j0}z_{j0} - {y_{j0}}^2 - {z_{j0}}^2 + R)^{\frac{1}{2}})/({k_1}^2 + {k_2}^2 + 1) \\ Y_j = k_1X_j + b_1 \\ Z_j = k_2X_j + b_2 \end{cases} \tag{17}$$

Where $k_1 = B_j/A_j$, $b_1 = y_{j0} - B_jx_{j0}/A_j$, $k_2 = C_j/A_j$, $b_2 = z_{j0} - C_jx_{j0}/A_j$, R is the polishing wheel radius.

The transformation matrix T shown in Eq. (13) is solved using Eq. (18):

$$T = \begin{bmatrix} a_x & b_x & c_x & p_x \\ a_y & b_y & c_y & p_y \\ a_z & b_z & c_z & p_z \\ 0 & 0 & 0 & 1 \end{bmatrix} = \begin{pmatrix} x_{tj} \\ y_{tj} \\ z_{tj} \\ 1 \end{pmatrix} \cdot \begin{pmatrix} x_{1j} \\ y_{1j} \\ z_{1j} \\ 1 \end{pmatrix}^{-1} \tag{18}$$

Optics EXPRESS

Finally, the relationship between the coordinates of the working point $t(x_t, y_t, z_t)$ of the polishing wheel and the position $B_1(x_1, y_1, z_1)$ is determined, as shown in Eq. (19). The coordinates of the working point $t(x_t, y_t, z_t)$ of the polishing wheel can only be determined by measuring the coordinates of the position $B_1(x_1, y_1, z_1)$.

$$\begin{pmatrix} x_t \\ y_t \\ z_t \\ 1 \end{pmatrix} = T \cdot \begin{pmatrix} x_1 \\ y_1 \\ z_1 \\ 1 \end{pmatrix} = \begin{pmatrix} x_{tj} \\ y_{tj} \\ z_{tj} \\ 1 \end{pmatrix} \cdot \begin{pmatrix} x_{1j} \\ y_{1j} \\ z_{1j} \\ 1 \end{pmatrix}^{-1} \cdot \begin{pmatrix} x_1 \\ y_1 \\ z_1 \\ 1 \end{pmatrix} \tag{19}$$

3.2. Elimination of measurement error

The position of the polishing wheel theoretical working point $t(x_t, y_t, z_t)$ is determined using Eq. (19). It is difficult for the normal line of the transition plate to pass through the centre point and working point of the polishing wheel simultaneously. Therefore, the coordinate of the working point $t(x_t, y_t, z_t)$ of the polishing wheel contains measure error, which will interfere with the judgment of the robot-MRF trajectory error information and needs to be removed. Because of the error caused by the measurement method, a Z-direction measurement error elimination model was established based on the constraint condition that the trajectory is aberration-free. According to the measured trajectory information, the measurement error is decoupled, as shown in Eq. (20).

$$\begin{cases} p = (X_{len}/X_{tlen} + Y_{len}/Y_{tlen})/2 \\ \Delta Z_i = pZ_i - Z_{ti} - \frac{1}{n}\sum_{i=1}^{n}(pZ_i - Z_{ti}) \\ m = \Delta Z_i \cdot [X_{ti}; Y_{ti}; 2{X_{ti}}^2 + 2{Y_{ti}}^2 - 1; 2X_{ti}Y_{ti}; {Y_{ti}}^2 - {X_{ti}}^2; 3{X_{ti}}^3 - 2X_{ti} + 3X_{ti}{Y_{ti}}^2; \\ \quad 3{Y_{ti}}^3 - 2Y_{ti} + 3{X_{ti}}^2Y_{ti}; 1 - 6{X_{ti}}^2 - 6{Y_{ti}}^2 + 6{X_{ti}}^4 + 12{X_{ti}}^2{Y_{ti}}^2 + 6{Y_{ti}}^4]^{-1} \\ \Delta Z_i' = \Delta Z_i - m \cdot [X_{ti}, Y_{ti}, 2{X_{ti}}^2 + 2{Y_{ti}}^2 - 1, 2X_{ti}Y_{ti}, \\ \quad {Y_{ti}}^2 - {X_{ti}}^2, 3{X_{ti}}^3 - 2X_{ti} + 3X_{ti}{Y_{ti}}^2, 3{Y_{ti}}^3 - 2Y_{ti} + 3{X_{ti}}^2Y_{ti}, \\ \quad 1 - 6{X_{ti}}^2 - 6{Y_{ti}}^2 + 6{X_{ti}}^4 + 12{X_{ti}}^2{Y_{ti}}^2 + 6{Y_{ti}}^4]^T \end{cases} \tag{20}$$

Where X_{len} and Y_{len} represent the measured distances in the X and Y directions, respectively; X_{tlen} and Y_{tlen} represent theoretical distances in the X and Y directions, respectively; Z_i and Z_{ti} represent the measured and theoretical trajectory coordinates of the corresponding point $(X_{ti,}Y_{ti})$ in the Z direction, respectively; m represents the measurement error proportion weight matrix; and $\Delta Z_i'$ represents the Z-direction trajectory error of robot-MRF excluding the measurement error.

To analyse whether the measurement error compensation model can accurately eliminate the measurement error in the Z-direction, the following example is used to judge the compensation accuracy of the measurement error compensation model. First, the trajectory error data in a plane with a diameter of ϕ380 mm is measured in the robot-MRF working area. The running track was a raster path with a step $\Delta X = 4$ mm and line spacing $\Delta Y = 4$ mm, and the sampling interval was 4 mm. The trajectory error and measurement error were characterized by PV of their data, as shown in Eq. (21). The measurement results were shown in Fig. 9 (a). The corresponding measurement error was calculated from the Z-axis trajectory error of the plane, as shown in Fig. 9 (b). The coordinates of the position $B_1(x_1, y_1, z_1)$ measured using the laser tracker can be regarded as the working point coordinates $t(x_t, y_t, z_t)$ of the polishing wheel. As a result, the

Optics EXPRESS

measurement error is primarily from the laser tracker (FARO ION, 16 μm + 0.8 μm/m). We can see of the form Fig. 9 (b) that the error in the measurement is $PV = 7$μm, who proved that the compensation accuracy of the measurement error elimination model in the Z direction is about 7μm, which is limited by the measurement precision of the laser tracker. Subsequently, the trajectory error information was measured in the sphere in which the robot-MRF ran the same trajectory and the same data collection interval in the same X-Y area. The measurement results and measurement error were shown in Fig. 10 (a) and Fig. 10 (b), respectively. It proved there was a measurement error when position $B_1(x_1, y_1, z_1)$ is directly converted to the working point $t(x_t, y_t, z_t)$ of the polishing wheel, and it is necessary to eliminate the measurement error. Simultaneously, the measurement error was again calculated on the basis of the trajectory error data with no measurement error (as shown in Fig. 10 (c)), and the result of verifying the accuracy of the measurement error removal was shown in Fig. 10 (d), $PV = 8$μm. Thus, one can see the form Fig. 10 (d) that when the measurement error was effectively removed, the trajectory error result did not contain any measurement error.

$$PV = \max(\Delta Z) - \min(\Delta Z) \tag{21}$$

Where ΔZ is the error data.

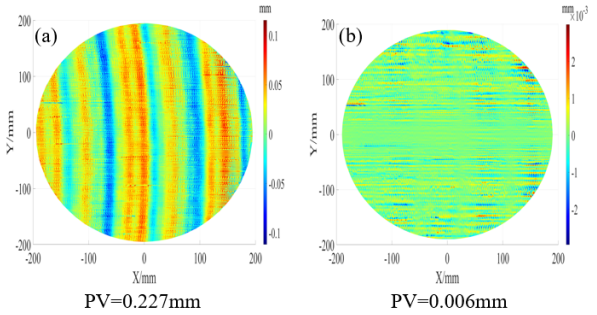

Fig. 9. Measurement results of Z-axis trajectory error in ϕ380 mm plane. (a) The plane measurement result, (b) the verification of compensation accuracy of the measurement error compensation model.

3.3. Analysis of trajectory error characteristics

It can be seen directly from Fig. 9 (a) and Fig. 10 (c) that there is a systematic Z-axis trajectory error of a period along the X-axis. To describe the performance characteristics of the Z-axis trajectory error, the corresponding Z-axis track errors along $Y = 0$ and $X = 0$ are extracted, and the corresponding 2-D trajectory errors and PSD curves are shown in Fig. 11.

Combined with Fig. 11(a) and Fig. 11(b), Z-axis systematic trajectory errors along the X-axis are divided into two types: one is short space periodic systematic error $T_1 \approx 24$ mm, $PV \approx 0.06$ mm, and data distribution in the red box as shown in Fig. 11(a); another is larger and longer space periodic systematic error, $T_2 \approx 64$ mm, $PV \approx 0.10$ mm, and shows data distribution in the green box as shown in Fig. 11(a). The error along the Y-axis ($X = 0$) shows a form of corrugated oscillation, $PV_{max} \approx 0.05$ mm, and the spatial period is related to ΔY. The positions of the wave peaks and valleys are related to the movement direction of the robot along the X-axis. When the robot moves from the negative X direction to the positive X direction, the entire trajectory line is usually located at the peak of the wave in the Y-axis direction; otherwise, it is located at the valley position. This indicates that the representation of the Z-axis trajectory error is related to the design of the trajectory.

Optics EXPRESS

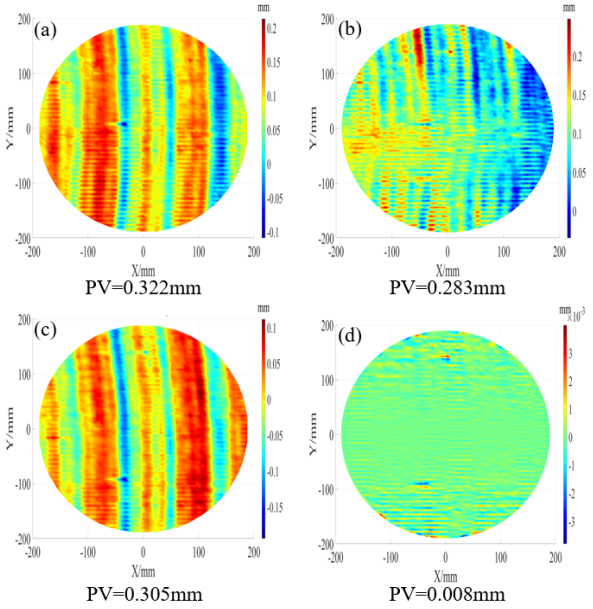

Fig. 10. The measurement results of Z-axis trajectory error in ϕ380 mm sphere. (a) The measurement result contains measurement error, (b) the sphere measurement error of Z-axis trajectory error, (c) the measurement result does not contain measurement error, (d) the measurement error elimination accuracy verification.

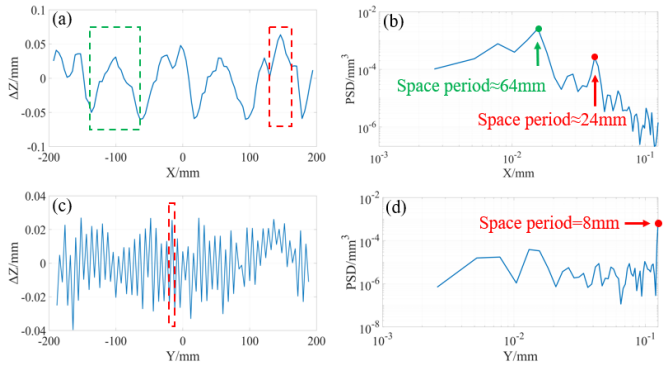

Fig. 11. The Z-axis trajectory error and PSD curves along X-axis and Y-axis. (a) The Z-axis trajectory error along the X-axis, (b) the PSD curve of Z-axis trajectory error along the X-axis, (c) the Z-axis trajectory error along the Y-axis, (d) the PSD curve of Z-axis trajectory error along the Y-axis.

Optics EXPRESS

In addition, the Y-axis track error along $Y = 0$ is extracted, and the corresponding 2-D trajectory error and PSD curve are shown in Fig. 12. The Y-axis trajectory error along the X-axis has a periodic systematic error $T_2 \approx 65$ mm and $PV \approx 0.10$ mm, which is very similar to the Z-axis systematic trajectory error. The X-axis trajectory error was also close to the Y-axis in the PV [34]. Therefore, the PV of the X-, Y-, and Z-axis trajectory errors can be approximated as $|\Delta x| = |\Delta y| = |\Delta z| < 0.2$ mm. According to Fig. 5, it can be concluded that during $\arcsin(D/2R) = \arcsin(1/2R^{\#}) \leq 15°$, the Z-axis trajectory error is the most important factor affecting the variation in the polishing gap. Accurate compensation of the Z-axis trajectory error is the primary task for obtaining a high-precision trajectory of the robot-MRF. Simultaneously, the Z-axis trajectory error with a space period of 4 mm was extracted, as shown in Fig. 13, indicating that in addition to systematic trajectory error, random trajectory error also existed, with $PV = 0.072$ mm < 0.1 mm and spatial period $T_3 \leq 4$ mm(because the sampling interval was 4 mm, the main frequency bands of random trajectory error were not reflected in the PSD curves of Fig. 11(b) and Fig. 11(d)). This further indicated that it is difficult to further improve the trajectory accuracy to less than 0.1 mm because the random error was the main component of the trajectory error.

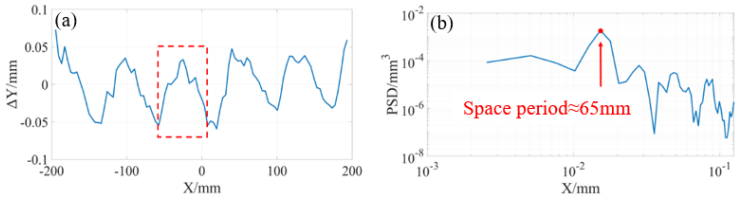

Fig. 12. The Y-axis trajectory error and PSD curve along X-axis. (a) The Y-axis trajectory error along the X-axis, (b) the PSD curve of Y-axis trajectory error along the X-axis.

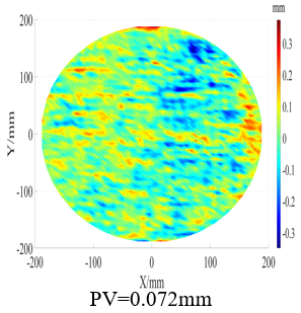

Fig. 13. The distribution of Z-axis random trajectory error.

4. Step-by-step and multistage iterations trajectory error compensation method based on spatial similarity

The trajectory error of robot-MRF comes from three parts: the robot module, the vibration disturbance of the magnetorheological module during operation, and the change of reaction force between the mirror and the polishing tool in the polishing process. The actual polishing process was performed by superimposing the vibration perturbation during the operation of the magnetorheological module on top of the robot module, and the error in the trajectory under the combined action of the two caused a constant change in the reaction force. The gravity component of the polishing tool changed at the same time at different orientations and each

Optics EXPRESS

trajectory point was rotating at a different velocity. At the end of the robot-MRF, the transient change in force and velocity had a novel effect on the robot's trajectory error. As a result, all three errors were coupled together, and it is very difficult for the model to accurately describe the robot-MRF trajectory error in the polishing process. However, based on the absolute error transfer relationship, the robot-MRF trajectory error in the polishing process can be expressed by Eq. (22):

$$PV_{rm} = PV_r + PV_{vd} + PV_{rf} \tag{22}$$

Where PV_r, PV_{vd}, *and* PV_{rf} are the trajectory errors PV of the robot module, the vibration disturbance of the magnetorheological module during operation, and the change of reaction force between the mirror and the polishing tool in the polishing process, respectively. They can be represented by Eq. (23):

$$\begin{aligned} PV_r &= PV_r' + PV_r'' = (\max(\Delta Z_r') - \min(\Delta Z_r')) + (\max(\Delta Z_r'') - \min(\Delta Z_r'')) \\ PV_{vd} &= PV_{vd}' + PV_{vd}'' = (\max(\Delta Z_{vd}') - \min(\Delta Z_{vd}')) + (\max(\Delta Z_{vd}'') - \min(\Delta Z_{vd}'')) \\ PV_{rf} &= PV_{rf}' + PV_{rf}'' = (\max(\Delta Z_{rf}') - \min(\Delta Z_{rf}')) + (\max(\Delta Z_{rf}'') - \min(\Delta Z_{rf}'')) \end{aligned} \tag{23}$$

Where $\Delta Z_r'$, $\Delta Z_{vd}'$, and $\Delta Z_{rf}'$ represent the systematic error in the trajectory of these three error parts respectively. $\Delta Z_r''$, $\Delta Z_{vd}''$, and $\Delta Z_{rf}''$ are the random error in the trajectory of these three error parts respectively.

To decompose and compensate the influence of each module of robot-MRF, a step-by-step and multistage iterations compensation method of robot-MRF Z-direction trajectory error was built based on spatial similarity of the trajectory error to obtain a high-precision trajectory. The measurement and compensation of the robot-MRF trajectory error can be divided into three states: (a) no-loading mode, (b) loading mode, and (c) polishing mode, as shown in Fig. 14. The trajectory error measurement platform was used to accurately measure the running error of each trajectory point of robot-MRF in different states. The measured trajectory errors are corresponding to each theoretical trajectory point from point to point based on the principle of spatial similarity of trajectory errors, and then the error compensation of each trajectory point can be solved. The specific compensation process of trajectory error is shown as follows:

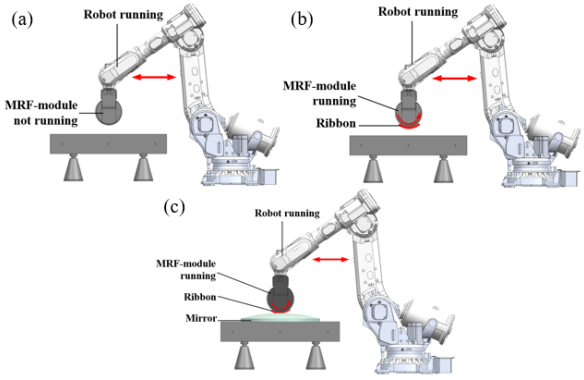

Fig. 14. The robot-MRF trajectory error of the three states. (a)No-loading mode: robot running but MRF module not, (b) loading mode: robot and MRF-module running but robot-MRF not polishing, (c) polishing mode: robot-MRF in polishing process.

First, the trajectory error of the robot-MRF in the no-loading mode is measured and compensated, which is aimed at the trajectory error compensation of the robot module. A theoretical trajectory (the number of trajectory points is usually in the tens of thousands to hundreds of thousands) was

Optics EXPRESS

generated based on the optical elements to be polished. The trajectory was run in the no-loading mode, and a laser tracker was used to continuously measure the trajectory error. However, due to the inconsistency between the measurement frequency and the step spacing or line spacing of trajectory points, as show in Fig. 15, the measured trajectory error points cannot correspond to the theoretical trajectory points one-to-one. To solve this problem, in this study, the linear triangulation interpolation method [35] was used to obtain the Z-axis trajectory error of the corresponding theoretical trajectory points based on spatial similarity of the trajectory error. The error compensation value of the corresponding theoretical trajectory point was obtained using Eq. (24). The trajectory error was compensated, and the compensated trajectory was measured again. If the systematic trajectory error in some areas is not completely suppressed after one-time compensation, the systematic trajectory error is dealt with by repeated measurement compensation until the systematic trajectory errors are effectively suppressed under the no-load condition.

$$\Delta z_i = Z_{ti} - \Delta Z_i' + \frac{1}{n}\sum_{i=1}^{n} \Delta Z_i' \tag{24}$$

Second, the trajectory error of the robot-MRF in loading mode is measured and compensated, which is aimed at trajectory error compensation with the MRF module working. Under the loading mode, the robot-MRF runs the trajectory after compensation in no-loading, and the z-axis track error is measured by the laser tracker. If there is a systematic trajectory error, it is compensated by iterative measurement and compensation until the systematic trajectory error is effectively suppressed in the loading mode.

Finally, the trajectory error of the robot MRF in the polishing mode was measured and compensated, which was aimed at the trajectory error compensation of the polishing process. When the robot-MRF is in the actual polishing process, the robot MRF is in a more complex state. In particular, due to the existence of orientation and trajectory errors, the surface reaction force between the mirror and the polishing tool is not constant, which has a certain influence on the force balance of each part of robot-MRF and may destroy the trajectory error that has been compensated in the loading mode. The trajectory error in the polishing process was measured using a laser tracker. By gradually correcting the trajectory error of the robot MRF during the polishing process, the trajectory accuracy can satisfy the requirements of MRF high-precision polishing and achieve high-precision manufacturing objectives.

The trajectory errors of the no-loading mode, loading mode, and polishing process were corrected step by step and multistage iteration using the trajectory error compensation method based on spatial similarity of the trajectory error, and the high-precision polishing requirements of the MRF were achieved. The advantage of this compensation method is that it can suppress the systematic trajectory error of the robot module and eliminate the systematic trajectory error caused by the operation disturbance of the MRF module and the change in reaction force between the mirror and polishing tool in the polishing process.

5. Trajectory error compensation and polishing verification

To verify the validity of the method of the robot-MRF, trajectory error compensation introduced above a ϕ340 mm fused silica plane mirror and a ϕ340 mm fused silica spherical mirror with a radius of 1207.67 mm were polished by the robot-MRF. The corresponding trajectory errors before and after the compensation and polishing results are as follows.

5.1. Build of robot-MRF

A robot-MRF was built, as shown in Fig. 16, to realise the combined application of MRF and robot. The robot is an ABB IRB 6700-200, with an operating range of 2.6 m, a loading of 200 kg, and a repeat positioning accuracy of ±0.05 mm. The MRF module weighed 107 kg,

Optics EXPRESS

and the diameter of the polishing wheel was 360 mm. Through precise TCP calibration, the position and orientation of the robot end and polishing wheel working point can be accurately converted. The rotation velocity of the polishing wheel was set at 60 rpm/min while the viscosity, maximum movement speed and flow rates of the MR fluids were constant at 15 Pa s,100 mm/s, and 1800 mL/min, respectively.

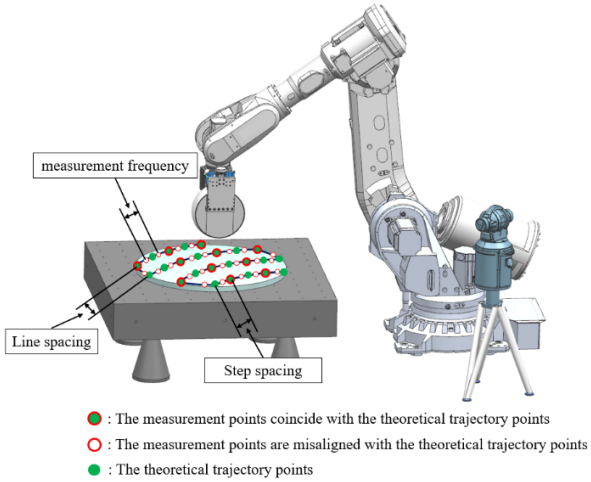

Fig. 15. The Schematic diagram of measured points do not correspond to the theoretical trajectory points.

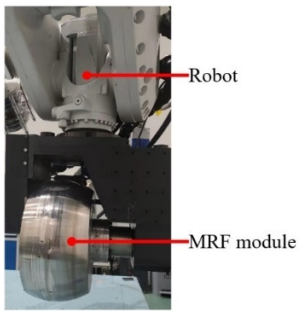

Fig. 16. The structure of the robot-MRF.

5.2. Trajectory error compensation and polishing of the plane mirror

5.2.1. Plane mirror trajectory error compensation by step-by-step and multistage iteration

Designed trajectory parameters and measured trajectory errors. The design of the raster trajectory with a diameter of ϕ380 mm, step spacing $\Delta X = 4$ mm, and line spacing $\Delta Y = 0.5$ mm. The trajectory error result in the no-loading mode was measured using a laser tracker, as shown in Fig. 17(a), with $PV_r = 0.227$ mm. The Z-axis track error after interpolation is shown in Fig. 17(b), with $PV = 0.216$ mm. The error data of the polishing track in the Z-axis corresponding along $Y = 0$ before and after interpolation were extracted, as shown in Fig. 18. In the effective working range ($|X| \leq 170$ mm), the interpolation and measurement results almost coincide; therefore, the error caused by interpolation can be ignored.

Optics EXPRESS

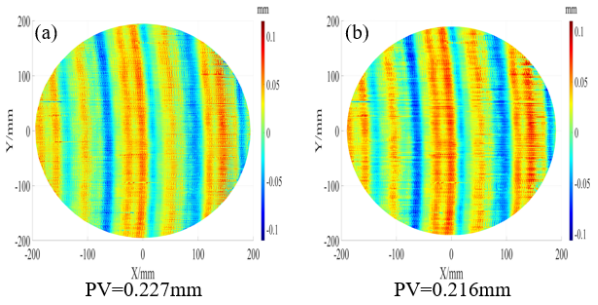

Fig. 17. The Z-axis trajectory error under no-loading. (a) Measurement results, (b) interpolation results.

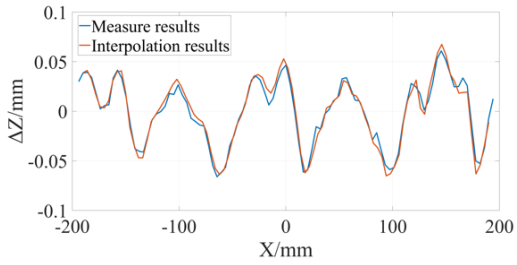

Fig. 18. Comparison of measured and interpolated Z-axis trajectory error.

The compensated trajectory was run, and the trajectory error was measured again. The Z-axis trajectory error is compensated two times by Eq. (24) in the no-loading mode, and the compensated trajectory error is PV_r''=0.074 mm, as shown in Fig. 19. It can be observed that the system trajectory error of the Z-axis of the robot without the MRF-module module is PV_r'=0.153 mm, and the compensation method can realise high-precision compensation of the Z-axis system trajectory error in the no-loading mode.

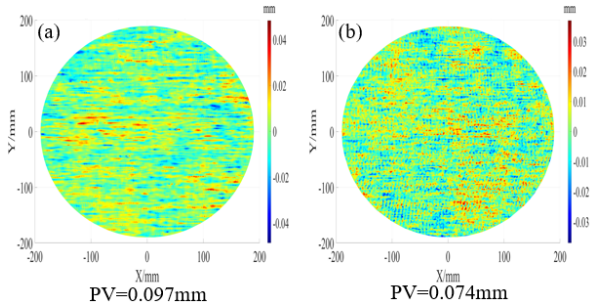

Fig. 19. Measurement results of Z-axis trajectory error after compensation under no-loading. (a) Measurement results of Z-axis trajectory error after first compensation, (b) measurement results of Z-axis trajectory error after second compensation.

The robot-MRF runs the polishing track under the loading condition (MRF-module operation), in which the polishing track is compensated in the no-loading condition, and the Z-axis track error is obtained under the loading condition of $PV = 0.085$ mm, as shown in Fig. 20(a). It was observed that under loading, the influence of the disturbance caused by the operation of

Optics EXPRESS

the MRF module on the overall trajectory error of the robot-MRF was mainly in the form of a random error, and the trajectory error $PV_{vd} = 0.011$ mm. Equation (24) was used to compensate for the trajectory error in this part. From the measurement results, as shown in Fig. 20(b), the compensated trajectory error is $PV = 0.080$ mm, whereas the systematic trajectory error is PV_{vd}'=0.005 mm, which is much smaller than that of the robot. It can be observed that the error compensation method can not only compensate for the partial trajectory errors of the robot but can also compensate for the trajectory error caused by the operation disturbance of the MRF module.

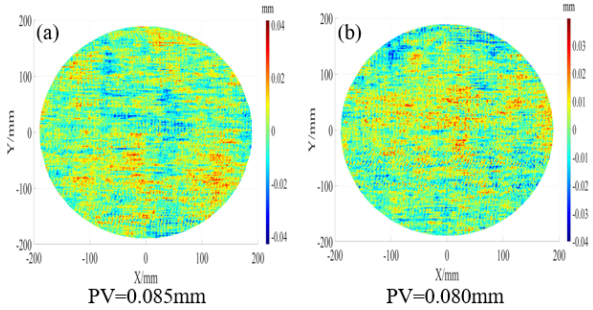

Fig. 20. Measurement results of Z-axis trajectory error under loading. (a) Measurement results of Z-axis trajectory error before compensation under loading, (b) measurement results of z-axis trajectory error after compensation under loading.

The trajectory errors of the robot MRF in the polishing condition were compensated. When the robot-MRF is in actual processing, the robot MRF is in a more complex state. In particular, due to the existence of orientation and trajectory errors, the surface reaction force of optical components is not constant [36,37], which has a certain influence on the force balance of each part of robot-MRF and may destroy the trajectory error that has been compensated in loading. By measuring the track error during the polishing process, the need for further compensation is judged. The Z-axis trajectory error during the polishing process is shown in Fig. 21(a) ($PV = 0.102$ mm). As shown in Fig. 21(a), the Z-axis trajectory errors in the red box are significantly higher than those in the other areas, which need to be further compensated. The trajectory error after the compensation is shown in Fig. 21(b), where $PV = 0.087$ mm. This indicates that the influence of the force changes on the trajectory error is mainly a systematic error: PV_{rf}'=0.015 mm, but this part of the error is still lower than the trajectory error caused by the robot. Simultaneously, Fig. 22 also showed that the systematic trajectory error of Z-axis with beyond 18 mm spatial period are effectively suppressed. The combined results in Fig. 21(b) indicate that the systematic trajectory error of the z-axis is accurately compensated.

$$\begin{cases} P_r = \frac{PV_r'}{PV_r'+PV_{vd}'+PV_{rf}'} \times 100\% \\ P_{vd} = \frac{PV_{vd}'}{PV_r'+PV_{vd}'+PV_{rf}'} \times 100\% \\ P_{rf} = \frac{PV_{rf}'}{PV_r'+PV_{vd}'+PV_{rf}'} \times 100\% \end{cases} \tag{25}$$

The trajectory error compensation method based on step-by-step and multistage iterations can realise high-precision compensation of the Z-axis systematic trajectory error of robot-MRF. Furthermore, the systematic trajectory error of the robot-MRF, which consists of a robot module, MRF-module disturbance, and reaction force between the mirror and polishing tool, is $PV' = PV_r' + PV_{vd}' + PV_{rf}' = 0.173$ mm. The systematic trajectory error caused by the robot is the most important component in the systematic trajectory error of the plane, PV_r'=0.153 mm,

Optics EXPRESS

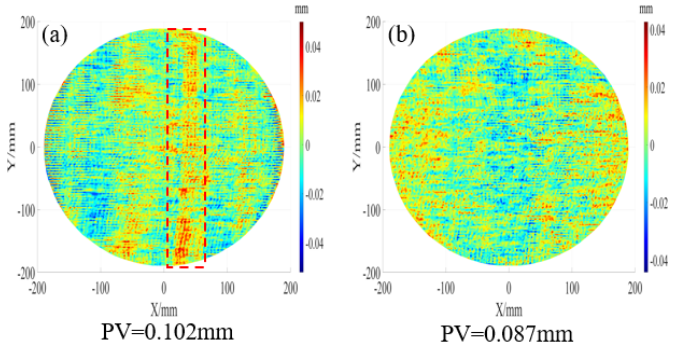

Fig. 21. Measurement results of Z-axis trajectory error under polishing process. (a) Measurement results of Z-axis trajectory error before compensation under polishing process, (b) measurement results of Z-axis trajectory error after compensation under polishing process.

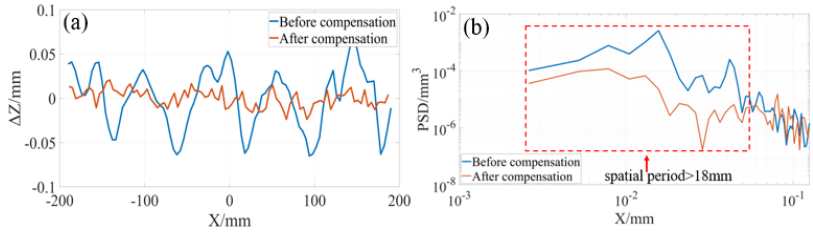

Fig. 22. Comparison of trajectory error before and after compensation of plane. (a) Comparison of the 2-D trajectory error before compensation in no-loading and after compensation in polishing process, (b) comparison of PSD curves of the 2-D trajectory error before compensation in no-loading and after compensation in polishing process.

which accounts for $P_r = 88.44\%$ according to Eq. (25). Followed by the influence of the reaction force changes in the polishing process, PV_{rf}'=0.015 mm, of which the proportion of systematic trajectory error is $P_{rf} = 8.67\%$ according to Eq. (25) . The disturbance of MRF-Module has little influence on the trajectory error, PV_{vd}'=0.005 mm, of which the proportion of systematic trajectory error is $P_{vd} = 2.89\%$ according to Eq. (25). Based on the above research, the advantages of this compensation method can be used to remove the process of compensating the trajectory error in the no-loading mode, directly compensating for the trajectory error in the loading mode, simplifying the compensation step, and shortening the compensation time.

5.2.2. Compensation accuracy comparison with model calibration method and non-model calibration method

At present, the model calibration method is the main method used for robot positioning and trajectory error compensation. Because of whether this method can achieve high-precision trajectory error compensation of the robot-MRF trajectory error, the CalibWare Software developed by ABB company was used to verify the trajectory error compensation accuracy of the robot-MRF, and the compensation results are shown in Fig. 23. It can be observed from Fig. 23(e) that compared with the distribution of the Z-axis random trajectory error before and after calibration, as shown in Fig. 23(b) and Fig. 23(d), the model calibration method compensates for the trajectory error to a certain extent; however, the original systematic Z-axis trajectory error is not effectively inhibited, as shown in Fig. 23(c) and Fig. 24. Therefore, it is difficult for the

Optics EXPRESS

model calibration method to achieve high-precision compensation for the trajectory error of a robot-MRF.

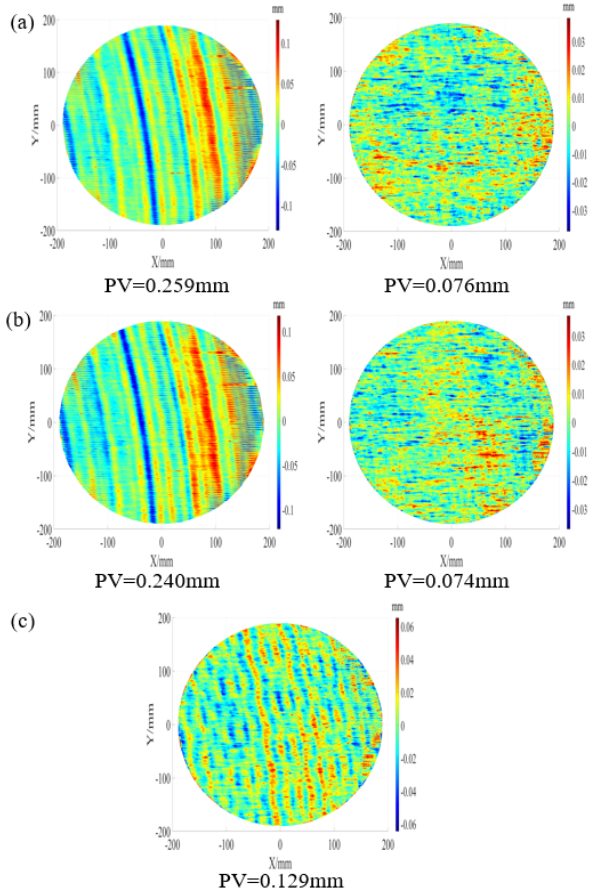

Fig. 23. The Z-axis trajectory error before and after calibration by the CalibWare Software. (a) The Z-axis trajectory error and random trajectory error before calibration by the CalibWare Software, (b) the Z-axis trajectory error and random trajectory error after calibration by the CalibWare Software, (c) the difference of Z-axis trajectory error before and after calibration by the CalibWare Software.

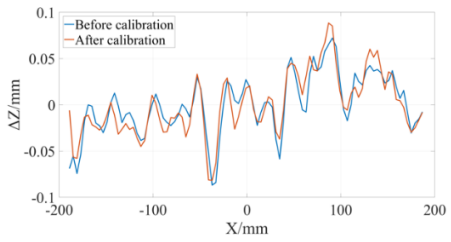

Fig. 24. The Z-axis trajectory error before and after calibration by the CalibWare Software along Y-axis.

Optics EXPRESS

The non-model calibration method is also a common compensation method for robot positioning and trajectory errors. Experimental verification is carried out in this study to verify whether this method can achieve high-precision trajectory error compensation for the robot-MRF trajectory error:

It is assumed that the position 500 mm above the centre point of the X-Y plane of the test bench is the centre point (0,0,0) of the measurement area, and the three concentric circles are Zone 1 (ϕ600 mm), Zone 2 (ϕ500 mm), and Zone 3 (ϕ400 mm). Raster tracks with the same step ($\Delta X = 4$ mm) and line spacing ($\Delta Y = 4$ mm) were run in each zone. The trajectory error of Zone 1 was measured using a laser tracker, and the sampling interval was 4 mm.

The trajectory errors in Zones 2 and 3 were extracted from Zone 1, and the error compensation of corresponding trajectory points in Zones 2 and 3 are calculated by using Eq. (24). The compensated polishing trajectories were run and measured in Zone 2 and 3, respectively. To avoid the influence of vibrations on the trajectory accuracy at the corner of the edge of the raster tracks, the compensated Z-axis trajectory errors of the central areas (ϕ300 mm) of the Zones 2 and 3 were extracted. The corresponding results are shown in Fig. 25. It can be observed from the measurement results that even for the same target points, the Z-axis trajectory errors of Zones 2, 3, and 1 in some regions are still quite different, which will have a certain influence on the polishing accuracy. Therefore, the non-model calibration method cannot achieve high-precision compensation for the trajectory error of a robot-MRF.

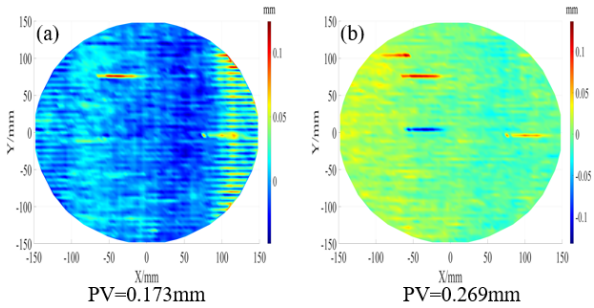

Fig. 25. The non-model method compensation results. (a) Zone 2 compensation results, (b) zone 3 compensation results.

5.3. *High-precision polishing experiment verification of plane mirror*

A polishing experiment was carried out on an outside diameter of ϕ340 mm and an inside diameter of ϕ60 mm plane mirror with the Z-axis trajectory error without compensation and compensation of the robot-MRF to verify whether the Z-axis trajectory error of the robot-MRF has been effectively compensated, and the robot-MRF with Z-axis trajectory error compensation has a high-precision polishing capability. The polishing parameters are listed in Table 1, and the initial surface accuracy of the plane mirror is shown in Fig. 26.

The polishing results of the plane mirror were shown in Fig. 27 when the Z-axis trajectory error is not compensated or compensated are shown in Fig. 24. To exclude the edge effect that influences the polishing results, areas beyond ϕ70 mm and within ϕ323 mm were selected as the polishing results. It can be observed from Fig. 27(a) that the polished surface has periodic errors caused by the Z-axis systematic trajectory error. When the Z-axis trajectory error was compensated, the final polishing result of the plane mirror reached 0.016λ, which can be considered as close-to-atomic scale [38]. Figure 28 also showed that after accurate calibration of the Z-axis trajectory error, the surface residuals beyond the 15 mm spatial period on the mirror surface are effectively suppressed, indicating that the systematic trajectory error of the Z-axis is

Optics EXPRESS

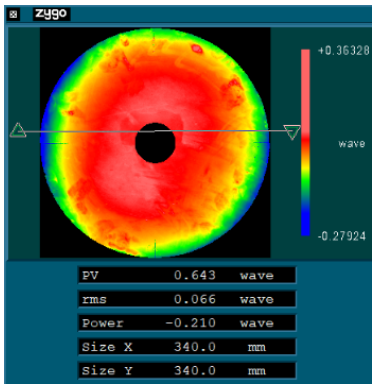

Fig. 26. The initial surface accuracy of plane mirror.

Table 1. The plane mirror polishing parameter table

parameter	plane mirror
material	fused silica
outside diameter	ϕ340mm
inside diameter	ϕ60mm
Initial surface error (RMS, λ=632.8 nm)	0.066λ
Grating track diameter	380mm
Grating track step ΔX	4mm
Grating track spacing ΔY	0.5mm
trajectory error before compensation (PV)	0.227mm
trajectory error after compensation (PV)	0.087mm

compensated accurately. The experimental results showed that the Z-axis trajectory error can be effectively compensated through the trajectory error compensation method based on step-by-step and multistage iterations, and the compensated robot-MRF has a high-precision polishing ability on plane mirrors. In addition, the results shown in Fig. 27(d) could be further improved, but the purpose of this experiment is to verify that the compensation method can suppress the influence of the systematic trajectory error of the robot on polishing accuracy. Subsequent spherical polishing experiments further explored the polishing capability of the compensated robot-MRF.

5.4. Trajectory error compensation and polishing of the spherical mirror

Experiments were carried out on a spherical mirror, which is a common curved element in optical systems to verify that the trajectory error compensation method is also applicable to the trajectory error of a curved surface and that the robot-MRF after compensation has the ability of high-precision polishing of curved surface components. The polishing parameters of the spherical mirror are listed in Table 2, and the initial surface accuracy of the plane mirror is shown in Fig. 29.

The measurement results of the trajectory error without the measurement error of the robot MRF at different stages are shown in Fig. 30. The measurement results showed that the trajectory error compensation method based on step-by-step and multi-stage iteration is also suitable for improving the polishing trajectory accuracy of a curved surface, and it can be observed from Fig. 31 that the systematic trajectory error of the spatial period greater than 18 mm is effectively suppressed. Furthermore, the systematic trajectory error of the sphere is PV'=0.263 mm, where

Optics EXPRESS

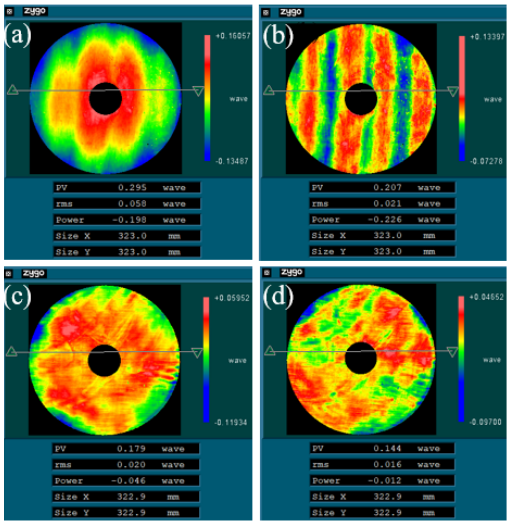

Fig. 27. The plane mirror polishing results of the robot-MRF (the area beyond ϕ70 mm and within ϕ323 mm). (a) First polishing results with systematic trajectory error: RMS = 0.058λ, (b) the first polishing results remove primary aberrations (Power, Coma, Astigmatism and Spherical aberration), (c) second polishing results without systematic trajectory error: RMS = 0.02λ, (d) third polishing results without systematic trajectory error: RMS = 0.016λ.

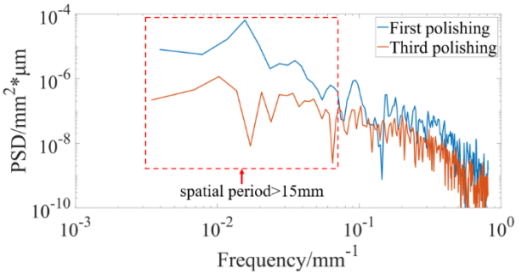

Fig. 28. The plane mirror PSD curves along the X-axis for the first and third polishing.

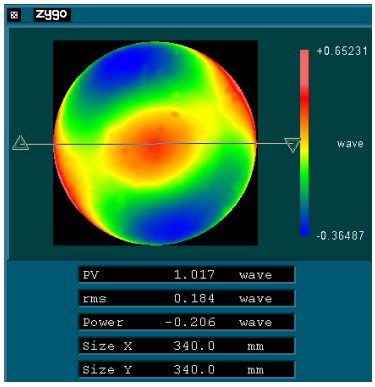

Fig. 29. Initial surface accuracy of spherical mirror.

Optics EXPRESS

Table 2. The spherical mirror processing parameter table

parameter	spherical mirror
material	fused silica
caliber	340mm
radius	1206.67mm
Initial surface error (RMS, λ=632.8 nm)	0.184λ
Grating track caliber	380mm
Grating track step ΔX	4mm
Grating track spacing ΔY	0.5mm
trajectory error before compensation (*PV*)	0.305mm
trajectory error after compensation (*PV*)	0.091mm

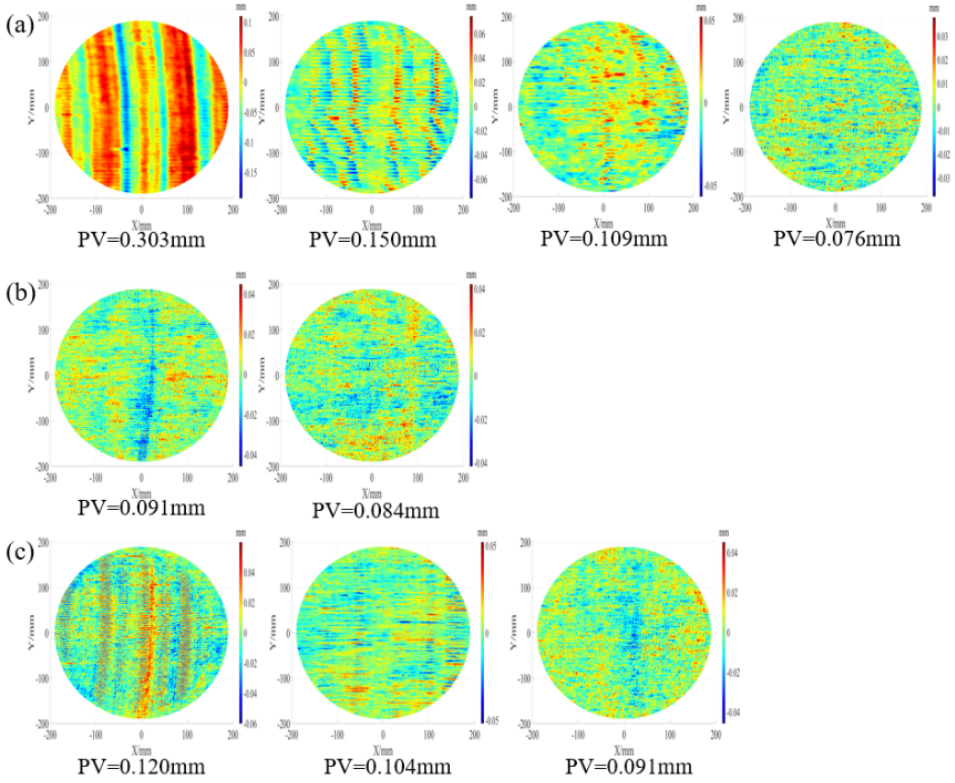

Fig. 30. Spherical mirror trajectory error without measure error. (a)The trajectory error before and after three times compensation under no-loading are respectively: $PV = 0.303$ mm and $PV = 0.076$ mm, (b) the trajectory error before and after compensation under loading are respectively: $PV = 0.091$ mm and $PV = 0.084$ mm, (c) the trajectory error before and after two times compensation under polishing are respectively: $PV = 0.120$ mm and $PV = 0.091$ mm.

Optics EXPRESS

the trajectory error caused by the robot is the most important component in the polishing trajectory error, PV_r'=0.227 mm, accounting for P_r = 86.31% of all the systematic trajectory errors of the robot-MRF using Eq. (25). Followed by the influence of the reaction force changes in the polishing process, PV_{rf}'=0.029 mm, of which the proportion of all the systematic trajectory errors is P_{rf} = 11.03% using Eq. (25). The disturbance of MRF-Module has little influence on the trajectory error, PV_{vd}'=0.007 mm, of which the proportion of all the systematic trajectory errors is P_{vd} = 2.66% using Eq. (25). Note that the trajectory error of the Z-axis was larger than that of the plane when the spherical surface was polished. This is because the robot-MRF only needs a three-axis linkage to polish a plane, whereas it needs at least a five-axis linkage for a sphere. Therefore, driving more axes to participate in the motion distribution leads to the introduction of more error sources, and more complex poses are more sensitive to changes in external forces.

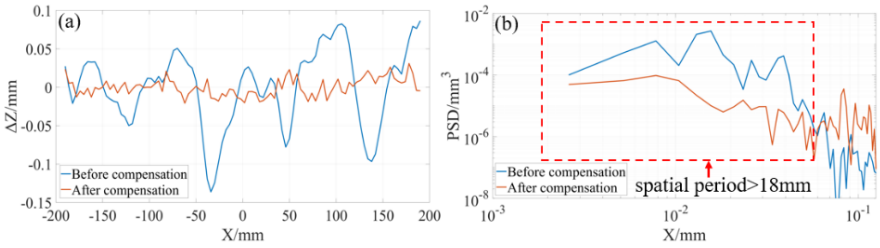

Fig. 31. Comparison of trajectory error before and after compensation of sphere. (a) Comparison of the 2-D trajectory error before compensation in no-loading and after compensation in polishing process, (b) comparison of PSD curve of the 2-D trajectory error before compensation in no-loading and after compensation in polishing process.

Using the compensated robot MRF, the surface error of the spherical mirror is polished from 0.184λ to RMS = 0.013λ, as shown in Fig. 32. The uncompensated track error and final processing results were normalised, and the corresponding PSD curves are shown in Fig. 33. It can be observed that in the final polishing results, the PSD curve corresponding to the surface residual error with a spatial period greater than 18 mm is less than the PSD curve corresponding to the uncompensated trajectory error, indicating that the trajectory error has been accurately compensated in the polishing process, and the compensated robot MRF can achieve high-precision polishing on curved surfaces.

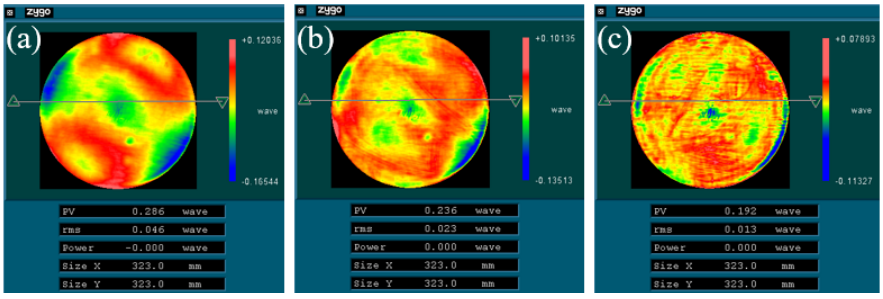

Fig. 32. Spherical mirror polishing results (95% of full aperture:323 mm). (a) first polishing results: RMS = 0.046λ, (b) second polishing results: RMS = 0.023λ, (c) third polishing results: RMS = 0.013λ.

Optics EXPRESS

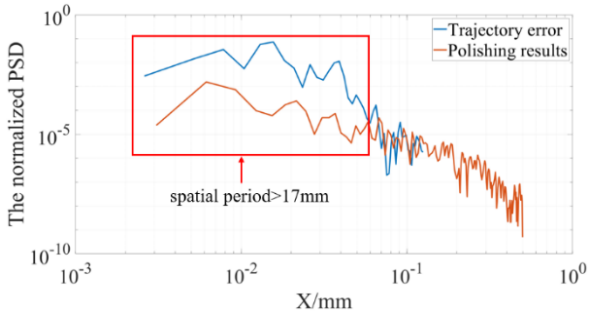

Fig. 33. The PSD curves of the normalized uncompensated trajectory error and the normalized final polishing results.

6. Conclusion

In this paper, the effects of position/orientation errors on the polishing gap were analyzed, and a continuous high-precision spatial dynamic measurement system was constructed to obtain an accurate measurement of the trajectory errors. A step-by-step and multistage iterations compensation method of robot-MRF Z-direction trajectory error was built based on spatial similarity of the trajectory error to obtain a high-precision trajectory. The polishing experiments proved that the compensated robot-MRF has the ability of high-precision polishing. The conclusions are summarized as follows:

(1) The relationship between the position/orientation errors and the polishing gap is proposed for the first time. It is indicated that the position error is the main reason for the variation of polishing gap, and the influence of Z-axis trajectory error on the stability of polishing gap gradually increases with the decrease of steepness($arcsin(1/2R^{\#})$). When the optical element steepness is lower than 15°, the Z-axis trajectory error affects the polishing gap stability by more than 90%, which needs to be accurately measured and compensated.

(2) A continuous high-precision spatial dynamic measurement method for the Z-axis trajectory error of the robot-MRF was designed, and the measurement error was eliminated to obtain an accurate measurement of the Z-axis trajectory error. The measurement results showed that there are systematic error trajectory errors with space period of 24 mm and 64 mm in X-Z direction, and the systematic trajectory errors in Y-Z direction are related to the extension and retraction directions of robot-MRF along X-axis.

(3) In this study, a Z-axis systematic trajectory error compensation method based on step-by-step and multistage iterations was established to improve trajectory accuracy. The experiments show that compared with the general model calibration method and non-model calibration method, the trajectory error compensation method established in this study can accurately compensate for the Z-axis systematic trajectory errors of the robot-MRF, and the compensation accuracy can reach $PV < 0.1$ mm. Moreover, the systematic trajectory error caused by the robot is the most important part of all the systematic trajectory errors of the robot-MRF, accounting for more than 85%, followed by the change in reaction force in the polishing process, accounting for approximately 10%, and the disturbance of MRF-module has the least influence on the trajectory error, accounting for less than 5% that cannot be compensated and measured in subsequent practical applications.

(4) High-precision polishing experiments were carried out on a ϕ340 mm fused silica plane mirror and spherical mirror with a radius of 1207.67 mm using the compensated robot-MRF.

Optics EXPRESS

The polishing results, the plane mirror polishing accuracy from 0.066λ RMS to 0.016λ RMS, and the spherical mirror polishing accuracy from 0.184λ RMS to 0.013λ RMS proved that the robot-MRF has the ability of high-precision processing and can be used in the field of high-precision optical polishing. These achievements have a great reference and promotion role for the application of robots in the field of high-precision optical manufacturing. However, the disadvantage of robot-MRF for high-precision polishing is that the Z-axis random trajectory error of robot-MRF induces the deterioration of medium- and high-frequency errors. The suppression of the Z-axis random trajectory error of the robot MRF is a topic to be explored in the future.

Funding. National Natural Science Foundation of China (11903035, 62275246, 12203048, 12003034); Youth Innovation Promotion Association of the Chinese Academy of Sciences (2021215).

Acknowledgments. The authors would like to thank the anonymous referees for their valuable suggestions and comments that have helped improve the paper.

Disclosures. The authors declare no conflicts of interest.

Data availability. Data underlying the results presented in this paper are not publicly available at this time but maybe obtained from the authors upon reasonable request.

References

1. H. M. Martin, R. Allen, V. Gasho, B. T. Januzzi, D. W. Kim, J. S. Kingsley, K. Law, A. Loeffa, R. D. Lutz, T. J. McMahon, C. J. Oh, M. T. Tuell, S. N. Weinberger, and S. C. West, "Manufacture of primary mirror segments for the Giant Magellan Telescope," Proc. SPIE **107060**, 30 (2018).
2. J. Vernin, C. Muñoz-Tuñón, M. Saranzin, H. V. Ramió, A. M. Varela, H. Trinquet, J. M. Delgado, J. J. Fuensalida, M. Reyes, A. Benhida, Z. Benkhaldoun, D. G. Lambas, Y. Hach, M. Lzarek, G. Lombardi, J. Navarrete, P. Recabarren, V. Renzi, M. Sabil, and R. Vrech, "European Extremely Large Telescope Site Characterization I: Overview," Publ. Astron. Soc. Pac. **123**(909), 1334–1346 (2011).
3. H. V. Ramió, J. Vernin, C. Muñoz-Tuñón, M. Saranzin, A. M. Varela, H. Trinquet, J. M. Delgado, J. J. Fuensalida, M. Reyes, A. Benhida, Z. Benkhaldoun, D. G. Lambas, Y. Hach, M. Lzarek, G. Lombardi, J. Navarrete, P. Recabarren, V. Renzi, M. Sabil, and R. Vrech, "European Extremely Large Telescope Site Characterization. II. High Angular Resolution Parameters," Publ. Astron. Soc. Pac. **124**(918), 868–884 (2012).
4. K. Kamikawa, A. Nagaia, T. Ashidaa, K. Tania, T. Nariyamaa, T. Ishidab, J. Takakib, N. Kawaguchib, M. Endob, Y. Ezakib, T. Usudac, and M. Saitoc, "High precision machining in TMT (Thirty Meter Telescope) structure manufacturing," Proc. SPIE **114451**, 267 (2020).
5. G. Derst and V. Giggel, "Fabrication technologies for large optical components at Carl Zeiss Jena GmbH," Proc. SPIE. **7739**, 773903 (2010).
6. D. Walker, C. Dunn, G. Yu, M. Bibby, X. Zheng, H. Wu, H. Li, and C. Lu, "The role of robotics in computer controlled polishing of large and small optics," Proc. SPIE. **9575**, 95750B (2015).
7. S. Wan, X. Zhang, M. Xu, W. Wang, and X. Jiang, "Region-adaptive path planning for precision optical polishing with industrial robots," Opt. Express **26**(18), 23782–23795 (2018).
8. S. Wan, X. Zhang, M. Xu, W. Wang, M. Xu, and X. Jiang, "Edge control in precision robotic polishing based on space-variant deconvolution," Precis. Eng. **55**, 110–118 (2019).
9. Z. Liu, B. Xie, and A. Wang, "The research of the precise aspheric wheeled polishing technology," Proc. SPIE. **10827**, 24 (2018).
10. B. Zhong, Q. Xu, J. Wang, W. Deng, and X. Chen, "Evaluation and compensation of a kinematic error to enhance prepolishing accuracy for large aspheric surfaces by robotic bonnet technology," Opt. Express **28**(17), 25085–25100 (2020).
11. M. Nouria, B. K. Fussella, B. L. Zinitib, and E. Linder, "Real time tool wear monitoring in milling using a cutting condition independent method," Int. J. Mach. Tools Manuf. **89**, 1–13 (2015).
12. B. Pan, R. Kang, Z. He, K. Li, Y. Zhang, W. Huang, and J. Guo, "Investigation of Deformation Mechanism and Suppression Method of Weak Stiffness Components by Magnetorheological Finishing," China Mechanical Engineering. **33**(18), 2190–2196 (2022).
13. X. Zhong, B. Fan, and F. Wu, "High-accuracy process based on the corrective calibration of removal function in the magnetorheological finishing," Opt. Eng. **56**(8), 084109 (2017).
14. K. Ren, X. Luo, L. Zheng, Y. Bai, L. Li, H. Hu, and X. Zhang, "Belt-MRF for large aperture mirrors," Opt. Express **22**(16), 19262–19276 (2014).
15. S. Wan, C. Wei, C. Hu, G. Situ, Y. Shao, and J. Shao, "Novel magic angle-step state and mechanism for restraining the path ripple of magnetorheological finishing," Int. J. Mach. Tools Manuf. **161**, 103673 (2021).
16. L. Ma, P. Bazzoli, P. M. Sammons, R. t. G. Landers, and D. A. Bristow, "Modeling and calibration of high-order joint-dependent kinematic errors for industrial robots," Robot. Cim-Int. Manuf. **50**, 153–167 (2018).

Optics EXPRESS

17. Y. Song, M. Liu, B. Lian, Y. Qi, Y. Wang, J. Wu, and Q. Li, "Industrial serial robot calibration considering geometric and deformation errors," Robot Cim-Int Manuf. **76**, 102328 (2022).
18. Y. Bai and D. Wang, "On the Comparison of Trilinear, Cubic Spline, and Fuzzy Interpolation Methods in the High-Accuracy Measurements," IEEE Trans. Fuzzy Syst. **18**(5), 1016–1022 (2010).
19. D. Chen, P. Yuan, T. Wang, Y. Cai, and L. Xue, "A Compensation Method for Enhancing Aviation Drilling Robot Accuracy Based on Co-Kriging," Int. J. Precis. Eng. Manuf. **19**(8), 1133–1142 (2018).
20. Y. Zeng, W. Tian, and W. Liao, "Positional error similarity analysis for error compensation of industrial robots," Robot Cim-Int Manuf. **42**, 113–120 (2016).
21. B. Li, W. Tian, C. Zhang, F. Hua, G. Cui, and Y. Li, "Positioning error compensation of an industrial robot using neural networks and experimental study," Chin. J. Aeronaut. **35**(2), 346–360 (2022).
22. G. Stefan, G. Hubert, M. Andreas, and N. Ronald, "Robot Calibration combining Kinematic Model and Neural Network for enhanced Positioning and Orientation Accuracy," IFAC-PapersOnLine. **53**(2), 8432–8437 (2020).
23. Y. Jiang, L. Yu, H. Jia, H. Zhao, and H. Xia, "Absolute Positioning Accuracy Improvement in an Industrial Robot," Sensors **20**(16), 4354 (2020).
24. G. Luo, L. Zou, Z. Wang, C. Lv, J. Ou, and Y. Huang, "A Robot Calibration Method Using a Neural Network Based on a Butter fly and Flower Pollination Algorithm," IEEE Trans. Ind. Electron. **69**(4), 3865–3875 (2022).
25. W. Wang, W. Tian, W. Liao, B. Li, and J. Hu, "Error compensation of industrial robot based on deep belief network and error similarity," Robot. Cim-Int. Manuf. **73**, 102220 (2022).
26. Y. Guo, S. Yin, Y. Ren, J. Zhu, S. Yang, and S. Ye, "A multilevel calibration technique for an industrial robot with parallelogram mechanism," Precis. Eng. **40**, 261–272 (2015).
27. X. Cheng and M. Zhao, "The Inverse Solution Algorithm and Trajectory Error Analysis of Robotic Arm Based on MQACA-RBF Network," J. Robotics **2020**, 1–11 (2020).
28. L. Biagiotti, L. Moriello, and C. Melchiorri, "Improving the Accuracy of Industrial Robots via Iterative Reference Trajectory Modification," IEEE Trans. Contr. Syst. Technol. **28**(3), 831–843 (2020).
29. B. Lin, X. Jiang, Z. Cao, and T. Huang, "Development and theoretical analysis of novel center-inlet computer-controlled polishing process for high-efficiency polishing of optical surfaces," Robot Cim-Int Manuf. **59**, 1–12 (2019).
30. J. Zhou and H. Kang, "A hybrid least-squares genetic algorithm–based algorithm for simultaneous identification of geometric and compliance errors in industrial robots," Adv. Mech. Eng. **52**(6), 1–12 (2016).
31. D. D. Walker, G. Yu, M. Bibby, C. Dunn, H. Li, H. Y. Wu, X. Zheng, and P. Zhang, "Robotic automation in computer controlled polishing," Adv. Mech. Eng. **11**, 16005 (2016).
32. R. Boby and A. Klimchik, "Combination of geometric and parametric approaches for kinematic identification of an industrial robot," Robot Cim-Int Manuf. **71**, 102142 (2021).
33. S. Aguado, J. Santolaria, D. Samper, J. J. Aguilar, and J. Velázquez, "Improving a real milling machine accuracy through an indirect measurement of its geometric errors," J Manuf Syst. **40**(1), 26–36 (2016).
34. G. Gao, G. Sun, J. Na, Y. Guo, and X. Wu, "Structural parameter identification for 6 DOF industrial robots," Mech. Syst. Signal Pr. **113**, 145–155 (2018).
35. I. Amidror, "Scattered data interpolation methods for electronic imaging systems: a survey," J. Electron. Imaging **11**(2), 157–176 (2002).
36. K. Xu, Y. Li, J. Zhang, and G. Chen, "ForceNet: An offline cutting force prediction model based on neuro-physical learning approach," J Manuf Syst. **61**, 1–15 (2021).
37. Y. Chang, J. Ding, Z. Hea, A. Shehzad, Y. Ding, H. Lu, H. Zhuang, P. Chen, Y. Zhang, X. Zhang, and Y. Chen, "Effect of joint interfacial contact stiffness on structural dynamics of ultra-precision machine tool," Int. J. Mach. Tools Manuf. **158**, 103609 (2020).
38. J. Gao, X. C. Luo, F. Z. Fang, and J. N. Sun, "Fundamentals of atomic and close-to-atomic scale manufacturing: a review," Int. J. Extrem. Manuf. **4**(1), 012001 (2022).